Human Exposure to EMFs from Wearable Textile Patch Antennas: Experimental Evaluation of the Ground-Plane Effect

Maria A. Seimeni[1, 2, *], Aris Tsolis[1],
Antonis A. Alexandridis[1], and Stelios A. Pantelopoulos[2]

Abstract—The aim of this paper is to prove that the power generated by a wearable textile patch antenna experiences reduced absorption in the phantom when the antenna ground-plane is increased. First, the dedicated human torso-equivalent phantom and two antennas were fabricated, which are multi-layered, with orientation normal to the body and made of the same materials. One of the antennas has a double in size ground-plane with regards to the other antenna, while the rest of their dimensions are identical. According to the proposed measurement procedure, once the radiation efficiencies of both antennas are measured in free space and with the phantom, the total absorption coefficient and the phantom losses are evaluated. The comparison of the measurement results proves that the increased ground-plane reduces the absorption on the phantom body of the antenna EM power (by 30.5%). Simulations and measurements were found in good agreement, with maximum deviation between the two up to 6% in terms of radiated efficiency. Hence, the proposed experimental evaluation of the impact of the ground-plane size of a wearable textile patch antenna on the reduction of the power absorbed by the user's body can be considered as a simple, reliable and cost-effective measurement method.

1. INTRODUCTION

Since the advent of modern wireless wearable systems applications, the public have been voicing their concerns about the potential deleterious effects of the electromagnetic fields (EMFs) on their health (e.g., general eye irritations and cataracts, cancer, etc.). Lately, due to the ever increasing wireless network densification, the exploitation of new frequency bands and the closer proximity of EMF sources (e.g., wireless devices and equipment, antenna, etc.) to the human body, the issue of the human exposure is brought up again seeking for updated answers.

Efforts in this direction have been carried out over the past 30 years. Nowadays, intense research on the biological effects of EM radiation and knowledge is more extensive than ever before. According to the existing literature, short-term low-level exposure at environmental or home levels does not lead to adverse effects. On the other hand, higher-levels (both short-term and long-term) of EM radiation that may cause unwanted effects are restricted by safety guidelines published by World Health Organization (WHO), International Commission on Non-Ionizing Radiation Protection (ICNIRP), Federal Communications Committee (FCC), and IEEE. What is disputed currently relates to the biological effects of the long-term low-level exposure of humans to EMFs radiation. The outcomes of the "International EMF Project" launched by WHO in 1996 do not confirm health consequences from exposure to low-level EMFs. However, some knowledge gaps, which require further investigation, exist.

Various methods of analyzing the exposure of the human body have been studied over the years. They involve both numerical simulations and experimental measurements. Thanks to EM simulators that apply numerical methods on phantoms representing the human body, the EM coupling of the radiating device to the biological tissues can be accurately simulated. If simulations are supported by the respective experimental setups, then realistic conclusions can be drawn for the human exposure to EMFs. Practically, lab experiments estimate human phantom exposure through direct Specific Absorption Rate (SAR) calculations using E-field probes [1, 2] and/or via thermographic cameras [3, 4]. However, these measurements demand dedicated equipment and accessories which, in total, cost a lot and require special laboratory facilities [1, 5, 6]. In light of these considerations, it is necessary to develop an experimental methodology that aligns as much as possible with the numerical results and leads to representative conclusions about EMF exposure.

In the same context, this paper primarily attempts to propose an efficient measurements procedure to assess the human exposure to EMF radiation generated by wearable textile antennas and, in light of this aim, to utilise far-field measurements facilities (not dedicated equipment for SAR measurements). The paper's main contributions are:

- *A simplified liquid torso-phantom.* The proposed phantom jointly encompasses merits such as ease of design and fabrication, easy-to-find ingredients and materials, equivalent electrical properties with the human body, etc.

- *An efficient textile patch antenna design technique to moderate human EMF exposure.* This design technique is effective and simple. It involves the resize (increase) of the ground plane of a textile patch antenna; hence it adds neither significant weight, nor significant manufacturing and material costs especially for the textile wearable antenna technology.

- An *efficient and reliable method to estimate the human exposure to EMFs sources.* This method is simple as it is based upon traditional antenna measurements; therefore, it can be followed with easy-to-find measurement equipment and measurement setups in a typical far-field antenna measurement test site (Anechoic chamber). It is worth noting that the method is easy to reproduce owning to the features and properties of the involved equipment. Apart from the standard instrumentation of a far-field antenna measurement site, extra specialized and expensive equipment are not involved; hence the measurements costs are maintained low.

This work is structured as follows: Section 2 presents various EMF exposure reduction techniques as a motivation of this work and our positioning. Section 3 describes the involved antenna system by providing the antenna design, the human-equivalent phantom liquid, as well as the phantom container and its supporting platform. The tests plan and tests setup are described in Section 4, while in Section 5 the performance of the antenna is presented. A discussion on the power absorbed by the phantom and the proposed measurements procedure is given in Section 6. Finally, Section 7 concludes this paper and is followed by the acknowledgements and the related literature.

2. HUMAN EMF EXPOSURE REDUCTION TECHNIQUES

Human exposure levels depend on several factors (operating frequency, field intensity, distance between antenna and user's body, exposure time, electric properties of the exposed body, etc.). If the status of at least one factor changes, then the human exposure levels change accordingly. For instance, the biological tissues experience a heat rise as the human body attempts to compensate and handle any extra amount of energy. A higher field intensity, a minimized distance between the biological tissue and the antenna, and the increased exposure time may jointly lead to higher exposure levels. Since it is not easy to prevent such a scenario from happening, different techniques are integrated in the antenna design so as to minimize the upcoming exposure. To the best of our knowledge, the most traditionally adopted techniques in portable/mobile antenna design are indicatively classified in: (i) those that control the direction of the radiation away from the human body [7–11]; (ii) those that shield the human body against the energy of the EMFs [12–18], whereas some of them are considered as very good candidates for wearable applications as well [19–26]. More specific and in terms of antenna structural changes, the classification of EMF reduction techniques becomes as follows: 1) parasitic element, 2) capacitive coupling elements, 3) slotted ground planes, 4) power divider, 5) ferromagnetic materials, 6) electrical

conductors below antenna as shield, 7) perfect magnetic conductors as a shield, 8) metamaterial surfaces as shield. In the following paragraphs, each technique is analytically presented.

In detail, in [7], a parasitic radiator is mounted on the front side of a printed circuit board (PCB) and shorted in the upper corners to cancel the near field that is generated by the antenna (mounted on the backside of the PCB) and impinges on the biological tissue. According to simulations, at 900 MHz SAR decreases by 27.5%, while at 1900 MHz peak SAR is not affected by the parasitic element. In [8], given that the device chassis operates as a significant radiator below 2 GHz, therefore effecting antenna operation, wave traps through capacitive coupling elements (CCE) are used to control current distribution on the chassis (near-field). Due to this fact, the near-field pattern maximum is moved away from the user's head, and the peak SAR value is decreased by 23% (top-mounted antenna) or even by 29.8% (bottom-mounted antenna). On the other hand, modifications of antenna geometry by slotting the ground plane are a very popular way to design handset antennas. In [9], first reports primarily pursued to improve antenna's bandwidth and efficiency using different slotted ground planes, while later studies examined the impact of the geometry of different radiating systems on SAR reduction [10]. Results demonstrated a SAR decrease up to 70% (bottom-mounted antenna) and 40% (top-mounted antenna). One major problem of this solution is the high frequency-selectivity of the slot that may release more EMF energy backwards towards the human body and this way lead to SAR levels increase. Moreover, controlling antenna pattern using dividing feed [11] is a solution used to weaken radiation toward the human body by controlling the direction of the radiation pattern through a power divider, a phase shifter, and a switch. In this case, reported SAR reduction equals 90%, while disadvantages are similar to those in the case of the parasitic element (requires space, careful design to avoid SAR increase, requires a phase shift feed per antenna element and extra switch).

By arranging Reflecting Elements [12] for mobile handsets between the human head phantom and the EMF source, a 20% increase in radiation efficiency and a 70%–80% decrease of SAR levels can be achieved. RF shields made of ferromagnetic material are used to reduce the back surface currents that cause the EMFs directed to the user. In some cases [13], SAR reduction equals 40%–57%, but the radiation efficiency was not jointly considered. In other studies, SAR reduction has been calculated equal to 25%–50% [14]. In these cases, even though the surface currents are reduced by the ferrite, the antenna efficiency is not affected appreciably. Given that Perfect Electric Conductors (PEC) do not naturally exist, conventional electrical conductors (EC) [15] are used as EM reflectors in many applications and are also used to investigate SAR response. In these studies, a non-connected sheet of EC with variable length is mounted below the antenna and PCB. Simulations indicate that EC's length is a very critical parameter for radiation efficiency, leading to slight improvement for short and long sheets and reduced efficiency for in-between lengths. SAR values for extreme EC length are decreased up to 50%, while for intermediate lengths demonstrate a double increase. When PEC's length is moderate, SAR levels increase, and antenna performance degrades; hence new surface materials are studied as shields. Perfect Magnetic Conductors (PMCs) would have been the perfect solution to significantly lower SAR levels. However, PECs and bulk PMCs are ideal materials which do not exist in nature, and artificial materials should be investigated and embedded in technology. Metamaterial surfaces (or metasurfaces) [16–18] have been taking-up since 1980 because they can inherently improve gain, bandwidth, directivity, and efficiency of the antenna, as well as reduce the size, sidelobes, and back-radiation of the antenna. They are all periodic arrays and patterns of metamaterial cells each resonating to a selected frequency to trap the EM energy, which otherwise would bounce on the human body and hence partially absorbed. Thanks to these mechanisms, antenna SAR values can be reduced up to 75% as reported by [16]. In [18], cell split resonators rings (SRRs) are embedded, human exposure can fall down by 27%–52%. In this study field, metamaterial/metasurfaces are classified in two groups: — (i) High Impedance Surfaces (HIS) such as the Artificially Magnetic Conductors (AMCs), (ii) Frequency Selective Surfaces (FSS) and Electromagnetic Band Gap (EBG) surfaces.

In an effort to reduce EMF exposure levels while maintaining acceptable antenna performance (to the best possible extent), low-profile antenna design, material, and fabrication low costs, the energy directed to the human body is chosen to be controlled through simple interventions in the antenna design. According to authors' previous work [27, 28], an effective and simple way to reduce the user exposure to the EMF of textile patch antennas is to increase the ground plane, as this technique adds neither significant weight, nor significant manufacturing and material costs.

3. SYSTEM DESCRIPTION

3.1. Antenna Designs

Based on the outcomes of our previous work [27, 28], in this paper we fabricate a textile microstrip patch antenna that is excited at a mode higher (TM21) than its fundamental TM10 (Textile Higher order Mode Microstrip Patch Antenna: Textile HMMPA) and therefore demonstrates a polarization with orientation normal to the human body. This type of antenna is appropriate for our study, because it:

- directs maximum radiation onto the body (used for on-body communications); hence human exposure to EMFs energy is significantly higher with regard to the antennas that exhibit polarization with orientation parallel to the body (off-body wireless communication links). In this way, the EM coupling between the phantom and the antenna can be studied more easily.
- encompasses wearability features (textile, low-profile, conformability-unobtrusiveness) owning to the combination of two technologies: this of the textile technology and that of the planar antenna technology.
- is simple to design and fabricate, and demonstrates good performance because of the microstrip structure.

In detail, the HMMPA is fabricated with dimensions that are tabulated in Table 1 and operates at 2.382 GHz. Hereinafter, the antenna model presented in Fig. 1 should be referred to as AM0 being the reference, initial antenna. The AM0 antenna is excited using proximity coupling technique and consists of multiple layers and three vias: a NoraDell conductive cloth ($h_t = 0.13$ mm, $\sigma = 1.54 * 10^7$ S/m) for the ground-plane, radiating patch and microstrip feedline; two felt substrates of different thicknesses ($h_{s1} = 2.9$ mm, $\varepsilon_{r1} = 1.23$, $\tan\delta_1 = 0.022$; $h_{s2} = 1$ mm, $\varepsilon_{r2} = 1.23$, $\tan\delta_2 = 0.022$); three wire vias (two ground vias, one feed via) made of copper (diameter: $D_f = 1.175$ mm and conductivity: $\sigma = 5.8 * 10^7$ S/m).

Table 1. HMMPA dimensions (mm).

$\mathbf{L_g = W_g = 50}$	$\mathbf{D_f = 1.175}$	$\mathbf{F_i = 25}$
$\mathbf{W_{felt} = 50}$	$\mathbf{h_{s,1} = 2.9}$	$\mathbf{D_y = 1}$
$\mathbf{W = 26.9}$	$\mathbf{h_{s,2} = 1}$	$\mathbf{D_{vias} = 4}$
$\mathbf{W_f = 4.2}$	$\mathbf{h_t = 0.1}$	

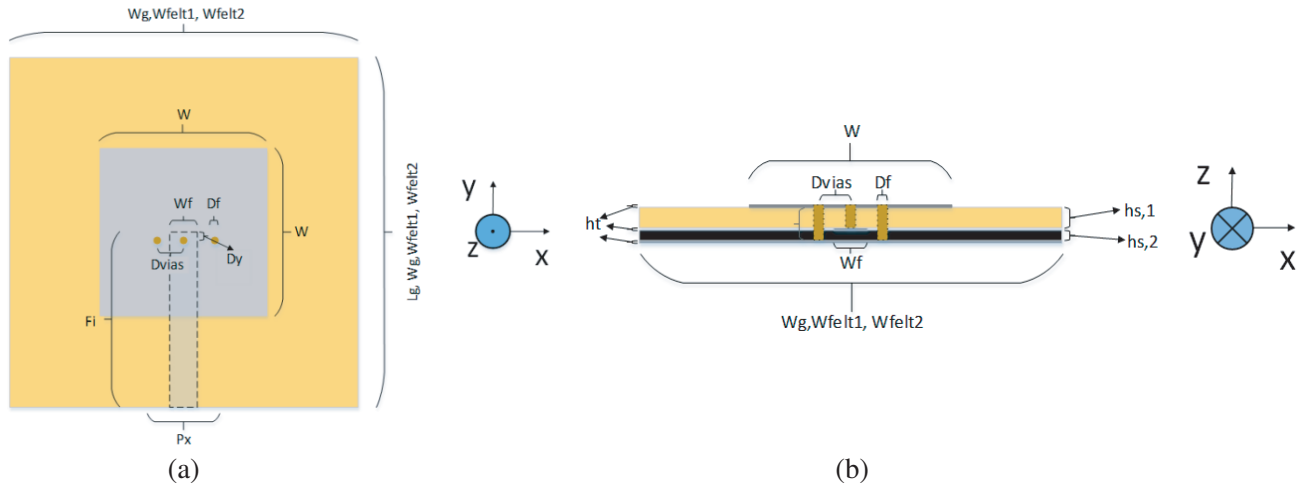(a)   (b)

Figure 1. Textile MPA (AM0$_{MPA}$ Reference Antenna) views: (a) Front (x-y plane) — and (b) bottom (x-z plane) — views.

Conclusions drawn from [27, 28], also, indicated that by increasing the ground-plane by ten steps of $n * \lambda/10$ (where $n = 1, 2, \ldots, 10$) [28], SAR level was decreased by 93% with regard to the SAR level of the initial design. Significant changes in human exposure were mostly obtained for $n = 1, 2, 3, 4, 5$. This is also visually presented in Fig. 2, where SAR is simulated on the 2/3-muscle human torso equivalent liquid phantom ($\varepsilon_r = 35.19$, $\sigma = 1.14\,\mathrm{S/m}$) for constant accepted power (0.5 Watts) [28]. Indeed, the SAR hotspots shrink as the ground plane increases. In this figure, it is obvious that SAR reduction is insignificantly decreasing for $n = 6, \ldots, 10$. For $n = 5$ (i.e., $\lambda/2$), SAR reduction equals 85.6% approximately. This antenna model (hereinafter AM5), which is double in size w.r.t. the ground-plane of AM0 (Fig. 3), worths further investigation and comparison with AM0 in terms of efficiency, human exposure, etc.
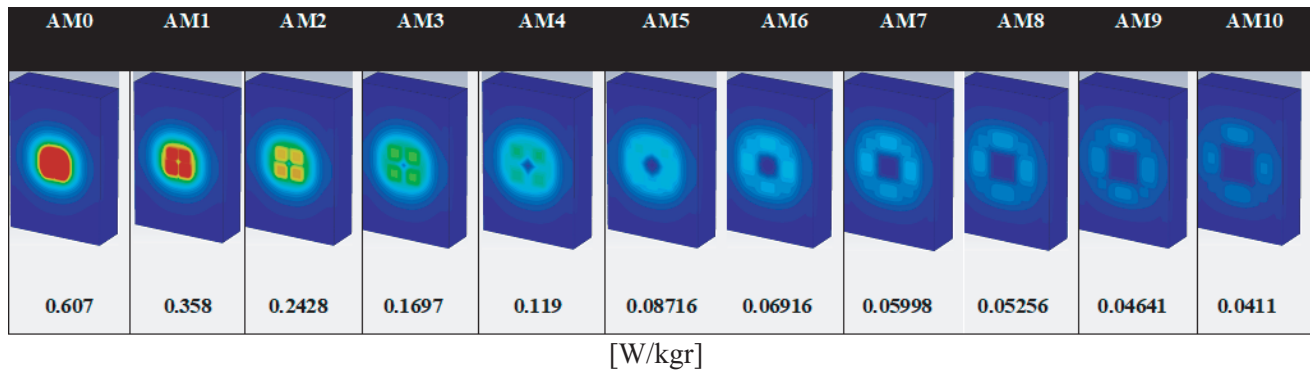

[W/kgr]

Figure 2. SAR (W/kgr) visualization per AM on the 2/3 human equivalent phantom ($\varepsilon_r = 35.19$, $\sigma = 1.14\,\mathrm{S/m}$). SAR is averaged over 10 grams of tissue at 2.4 GHz. The numbers denote maximum SAR value.
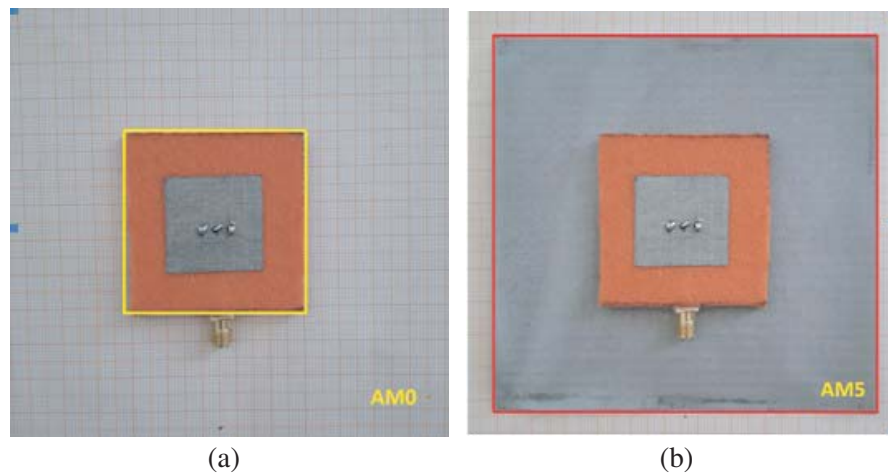

(a)   (b)

Figure 3. The fabricated antenna models: (a) AM0 and (b) AM5.

It must be noted that if the electrical conductivity of the phantom changes (e.g., increases), SAR values for each ground-plane change (e.g., increase) accordingly, while the absolute values of SAR reductions (%) do not change. The latter is justified by the fact that the size increments of the ground plane are the same. In this work, we are not interested in the absolute values of the SAR, rather we are interested in proving through measurements the reduction (%) of the absorbed power on the phantom relative to AM0.

3.2. Preliminary Considerations about Simulated Phantom Losses for All Antenna Models

A way to have an estimation of the EM exposure is through the losses that the phantom demonstrates (Fig. 4: red curve). Fig. 4 is obtained from [28] for a 2/3 muscle equivalent phantom. The losses represent the power absorbed by the biological tissue and are calculated by the EM simulation software (CST) as depicted in Fig. 5, which practically is a modification of the schematic diagram of the power balance representation provided by [29].
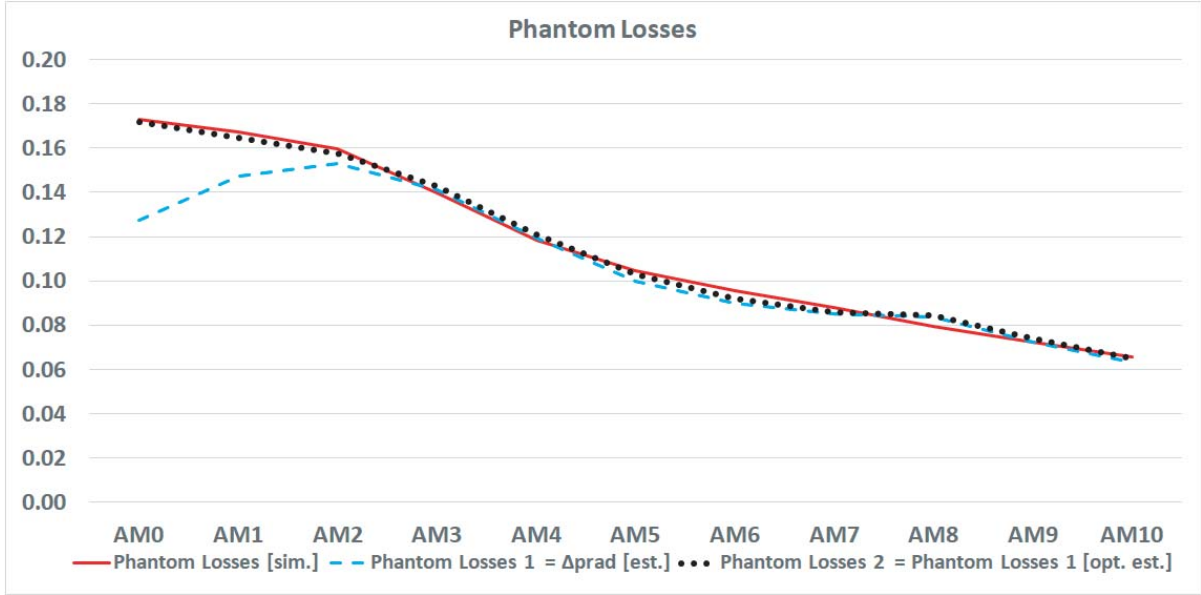

Figure 4. Human Phantom losses as calculated via EM simulations (solid curve). Estimated Phantom Losses is the difference between the Radiated Power with and without phantom (dashed curve). Optimized Estimated Phantom Losses includes HMMPA Losses and the Accepted Power with and without phantom (dotted curve). Values are obtained at 2.4 GHz.
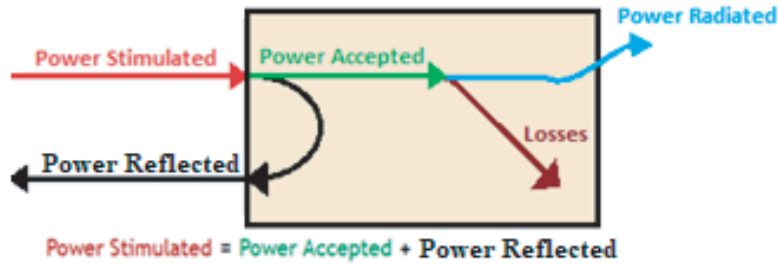

Figure 5. Schematic diagram of the power balance representation [29].

One would expect that the losses ($L_{Phantom}$) on the phantom equal the difference between the antenna radiation power with (P_{rad}^o) and without (P_{rad}^i) phantom:

$$L_{Phantom} = P_{rad}^i - P_{rad}^o \tag{1}$$

The superscripts in the above equation and elsewhere in the document hereinafter represent the two scenarios: without (^{i}) and on phantom (^{o}). According to Fig. 4, the red and blue curves do not overlap for AM0 up to AM2 models. The difference between the curves implies inaccuracy because

some parameters are not considered: the power accepted by the antenna port (P_{acc}) and the antenna losses (L_{HMMPA}).

To correlate the above mentioned parameters, the accepted power should be the sum of the radiated power and all losses of the system (antenna losses, phantom losses):

$$P_{acc} = P_{rad} + L = P_{rad} + L_{HMPPA} + L_{Phantom} \implies L_{Phantom} = P_{acc} - P_{rad} - L_{HMPPA} \tag{2a}$$

$$L_{HMPPA} = L_{Felt} + L_{Cu} + L_{NoraDell} \tag{2b}$$

where L are the system losses; L_{Felt} are the Felt losses (two substrates of the patch antenna); L_{Cu} are the Copper losses (wire vias); and $L_{NoraDell}$ are the Nora Dell conductive cloth losses (radiating element, feed line, ground plane). From Eq. 2(a), the following equations can be derived for the two scenarios (free space, on phantom):

$$L^i_{Phantom} = P^i_{acc} - P^i_{rad} - L^i_{HMPPA} \tag{3a}$$
$$L^o_{Phantom} = P^o_{acc} - P^o_{rad} - L^o_{HMPPA} \tag{3b}$$

where, obviously, $L^i_{Phantom} = 0$. Subtracting Eq. 3(a) from Eq. 3(b), Eq. (4) is derived:

$$\overset{3(b)-3(a)}{\implies} L^o_{Phantom} - L^i_{Phantom} = P^o_{acc} - P^o_{rad} - L^o_{HMPPA} - P^i_{acc} + P^i_{rad} + L^i_{HMPPA} \overset{L^i_{Phantom}=0}{\implies}$$

$$\mathbf{L^o_{Phantom}} = \left(\mathbf{P^i_{rad}} - \mathbf{P^o_{rad}}\right) + \left(\mathbf{L^i_{HMPPA}} - \mathbf{L^o_{HMPPA}}\right) - \left(\mathbf{P^i_{acc}} - \mathbf{P^o_{acc}}\right)$$

$$\implies \mathbf{L^o_{Phantom}} = \mathbf{\Delta P^{i,o}_{rad}} + \mathbf{\Delta L^{i,o}_{HMMPA}} - \mathbf{\Delta P^{i,o}_{acc}} \tag{4}$$

where $\Delta P^{i,o}_{rad}$ is the difference between the radiated powers without and with the phantom; $\Delta L^{i,o}_{HMMPA}$ is the difference between the losses of the antenna materials without and with the phantom; $\Delta P^{i,o}_{acc}$ is the difference between the accepted powers without and with the phantom. From Eq. (4), the black (dotted) curve occurs (Fig. 4) that better overlaps the red curve. The minor differences between the two curves may stem from calculation inaccuracies. The differences between the blue (dashed) and red (solid) curves could also be justified by the following claim: as the ground-plane becomes larger (AM3, ..., AM10), the induced currents in the torso which also radiate EMFs (scattering fields) towards the antenna and off the body are better blocked, while $\Delta L^{i,o}_{HMMPA}$ and $\Delta P^{i,o}_{acc}$ become insignificant; hence P_{acc} and L_{HMMPA} are not influenced by the human torso and remain quite unchanged.

3.3. Human Tissue Equivalent Liquid: Phantom

The requirement for simple, cost-effective and accurate experiments that reproduce real-case exposure scenarios to the best possible extent mandates — first of all — the identification of a suitable human torso-equivalent phantom. For this reason, we developed a customized solution regarding the phantom container and the liquid content. In this subsection, the human tissue — equivalent liquid mixture formula is described, while the container characteristics are provided in the next paragraph.

The physical and electrical properties of components that simulate biological organs were tabulated by Gabriel [30] through parametric modeling and can be obtained automatically thanks to the on-line application prepared by the Italian National Research Council [31]. These properties are achieved through a wide range of human tissue-equivalent mixtures, which are housed by enclosures that can be found in literature [32–36] and in market [5, 6]. The mixtures [32–34] are usually classified according to the number of tissue-layers (homogeneous: 1 tissue layer, heterogeneous: multiple tissue layers), base ingredient, and low/high-water content (e.g., liquid, gel, semi-solid, solid), etc., whereas containers ([5, 6, 32, 35, 36]) are classified according to their resemblance to the external envelope of the human body shape (e.g., anthropomorphic or physical models, canonical models), etc.

Ideal for our study would be a human-torso phantom that encompasses the following merits:

- Ease of design (reasonable computational resources and shape complexity) in simulations;
- Ease of fabrication and reproducibility (including fabrication costs);
- Stability of the electromagnetic and mechanical properties w.r.t. the duration of the experiment;
- EM equivalency with the part of the human body of interest.

Trying to jointly capture all above phantom merits, we have decided to develop a 2/3 muscle-equivalent homogeneous [30] rectangular phantom ($\varepsilon_r = 35.19$, $\sigma = 1.14\,\text{S/m}$, $\tan\delta = 0.24191$) made of simple and commonly used ingredients (e.g., salt, sugar). In [33], Castello-Palacios et al. propose to use a mathematical model to predict the composition for a tissue of known dielectric properties at 2.4 GHz. The model consists of two general formulas that provide the chemical formulation of the aqueous solution for given dielectric constant (ε_r) and electrical conductivity (σ). Hence, any pair of concentration, %wt, (c_{NaCl}, $c_{sucrose}$) of sodium chloride (salt, NaCl) and sucrose (sugar, $C_{12}H_{22}O_{11}$) can be obtained by solving the following linear system of equations:

$$\varepsilon'_r(c_{NaCl}, c_{sucrose}) = (0.01 \cdot c_{sucrose} - 2.633) \cdot c_{NaCl} - 0.007 \cdot c_{sucrose}^2 - 0.316 \cdot c_{sucrose} + 78.704 \quad (5)$$

$$\sigma(c_{NaCl}, c_{sucrose}) = (-0.029 \cdot c_{sucrose} + 1.604) \cdot c_{NaCl} + 0.021 \cdot c_{sucrose} + 1.533 \quad (6)$$

To synthesize, at the referred frequency, a muscle-equivalent liquid ($\varepsilon_r = 52.79$, $\sigma = 1.71\,\text{S/m}$, $\tan\delta = 0.24191$) according to Castello-Palacios, the liquid-phantom should consist of 41.53% sugar and 0% salt leading to electrical properties such as $\varepsilon_r = 50.97$ and $\sigma = 2.29\,\text{S/m}$ that deviate from the target values. Since we intend a 2/3 muscle-equivalent phantom, the sugar concentration should further increase, and this way decreases the dielectric constant to 35. By doing so, the salt concentration should be increased, so is the electrical conductivity. However, the latter is not desired as the electrical conductivity has to be lowered to $1.13\,\text{S/m}$. This can also be verified through calculations using the above equations. The closest achievable values that can be obtained through the equations for the electrical properties of the 2/3 human equivalent phantom are $\varepsilon_r = 30$ and $\sigma = 2.47\,\text{S/m}$ with 58.5%wt sugar and 3%wt salt. The achieved value for the dielectric constant deviates from the desired value by 5 units, whereas the value for the electrical conductivity deviates approximately $1.5\,\text{S/m}$. In [33], it is proved that for high sugar concentrations (as in our case), salt slightly increases the conductivity and decreases the dielectric constant. On the other hand, sugar decreases the dielectric constant without significant changes in the losses. Therefore, the achieved values for the 2/3 muscle equivalent phantom (58.5%wt sugar, 3%wt salt, 38.5% deionized water) are the closest possible choice to the desired values. To summarize the previous results, we create Table 2 which indicates the electrical properties of muscle as evaluated by Gabriel et al. [30] at 2.4 GHz, the electrical properties of the muscle-equivalent phantom that Palacios achieved in [33] through dedicated prediction formulas, the electrical properties of the 2/3 muscle that this paper targets to achieve, and finally, the electrical properties of the liquid solution that this paper achieved based on the Palacios formulas. Additionally and concluding from this section note that for reference and theoretical validity reasons EM simulations of an antenna on a torso-equivalent phantom demonstrating $\varepsilon_r = 30$ and $\sigma = 2.47\,\text{S/m}$ were also run in order to check differences in performance and SAR values. As expected, the higher electrical conductivity leads to higher exposure levels of one-order of magnitude, as described in the last paragraph of Section 3.1.

Table 2. Tissue electrical properties & phantom chemical concentrations at 2.4 GHz.

		Gabriel's Muscle [30] (target values)	Palacios' Muscle-equivalent Phantom [33] (achieved values)	2/3 Muscle (target values)	Palacios' 2/3 Muscle-equivalent Phantom (achieved values)
Electrical Properties	ε_r	52.79	50.97	35.19	30
	σ (S/m)	1.71	2.29	1.14	2.47
Chemical Concentrations (%wt)	Sugar		41.53		58.5
	Salt		0		3

As for the preparation of the phantom liquid, due to high-water content, special care is taken to avoid water evaporation. Phantom's ingredients are properly dissolved through intensive stirring, while water quantity remains constant. With the use of a bucket and a high accuracy weight scale, we prepare a solution weighting 31.167 kgr, consisting of 18.216 kgr of sugar, 0.951 kgr of salt, and 12 kgr of deionized water (Table 3). The solution is then poured in the phantom enclosure.

Table 3. Tissue electrical properties & phantom chemical concentrations at 2.4 GHz.

Ingredient	Chemical Concentration (%wt)	Weight (Kgr)
Sugar ($C_{12}H_{22}O_{11}$)	58.5	18.216
Salt (NaCl)	3	0.951
Deionized Water (H_2O)	38.5	12
TOTAL	100	31.167

3.4. Human Tissue Equivalent Liquid: Phantom

The dimensions of the internal volume of the phantom enclosure have been decided to equal the average dimensions of an adult torso, that is to say: $33\,cm \times 14\,cm \times 49\,cm$ [36]. The enclosure is made of Plexiglass ($\varepsilon_r = 2.36$, $\tan\delta = 1.62 * 10^{-3}$, thickness $= 6\,mm$). Given that we intend to measure the antenna radiation patterns for $\varphi = 0°$ (Fig. 6(a)) and $\varphi = 90°$ (Fig. 6(c)) but also for $\varphi = 45°$ (Fig. 6(b)) and $\varphi = 135°$ (Fig. 6(d)), a supporting platform (base and chocks) has been envisaged (Figs. 6(b) and 6(d) below). The platform is made of wood, is not expected to affect measurements, and is placed onto the turn-table in an anechoic chamber when the $45°$ and $135°$ azimuth (φ)-cut radiation patterns of the Antenna Under Test (AUT) have to be measured. In the pictures below, the AUT feeding cable position for each φ is presented. The trace of the dotted small rectangle coincides with the AM0-antenna's border, while the trace of the solid large rectangle corresponds to the AM5.

4. TEST PLAN AND TEST SET-UP

The test plan and test setup that are adopted include all the involved equipment gradually so that their contributions to the measurements are taken into consideration. In this way, any uncertainties inserted in the measurements by supporting materials (e.g., supporting platform, chocks) are removed during the measurements. The test setup is depicted in Fig. 7, while test procedure is summarized in Table 4. Fig. 8 shows the phantom in the anechoic chamber for the four φ positions. The phantom positioner is made of Styrofoam and wood, which are EM transparent materials.

In detail, AM0 and AM5 are positioned at 4.63 m distance from a calibrated probe antenna (Horn Antenna EMCO-3115). S_{11} and the four radiation patterns ($\varphi = 0°, 45°, 90°, 135°$) are recorded for each antenna model and for each scenario ("free space" and "on-phantom"). The turn-table is programmed by the positioning controller to execute one full step-wise θ angle rotation ($5°$ degrees steps); hence 72 samples of θ are collected per each φ value leading to a total number of 288 samples of radiation diagram for each antenna. These samples are used to calculate the total radiated power by each antenna (AM0, AM5) for each test case ("in free-space" and "on-phantom").

5. ANTENNA PERFORMANCE AND CHARACTERIZATION

In the previous section, it has been ascertained that the antenna demonstrating a polarization with orientation normal to the body (i.e., HMMPA) leads to higher user exposure to EMFs w.r.t. to the antenna with polarization parallel to the user's body. The purpose of this section is to investigate the means to reduce user's exposure to EMFs. Being the worst case scenario for human exposure, the HMMPA is selected for this purpose.

Following the above test plan, the two wearable textile antenna models (AM0, AM5) are first measured in free space and, then, on phantom inside the anechoic chamber (far-field measurements site). In Fig. 9, S_{11} is depicted for both antennas on Phantom. The radiation patterns ("in free-space" and "on-phantom") for both antennas AM0 and AM5 are presented in Fig. 10 and Fig. 11.

In detail, the operational frequency of the textile antenna models is confirmed for both by full 2-port S-parameters measurements with a VNA that is calibrated at the antenna's ports. In free space,
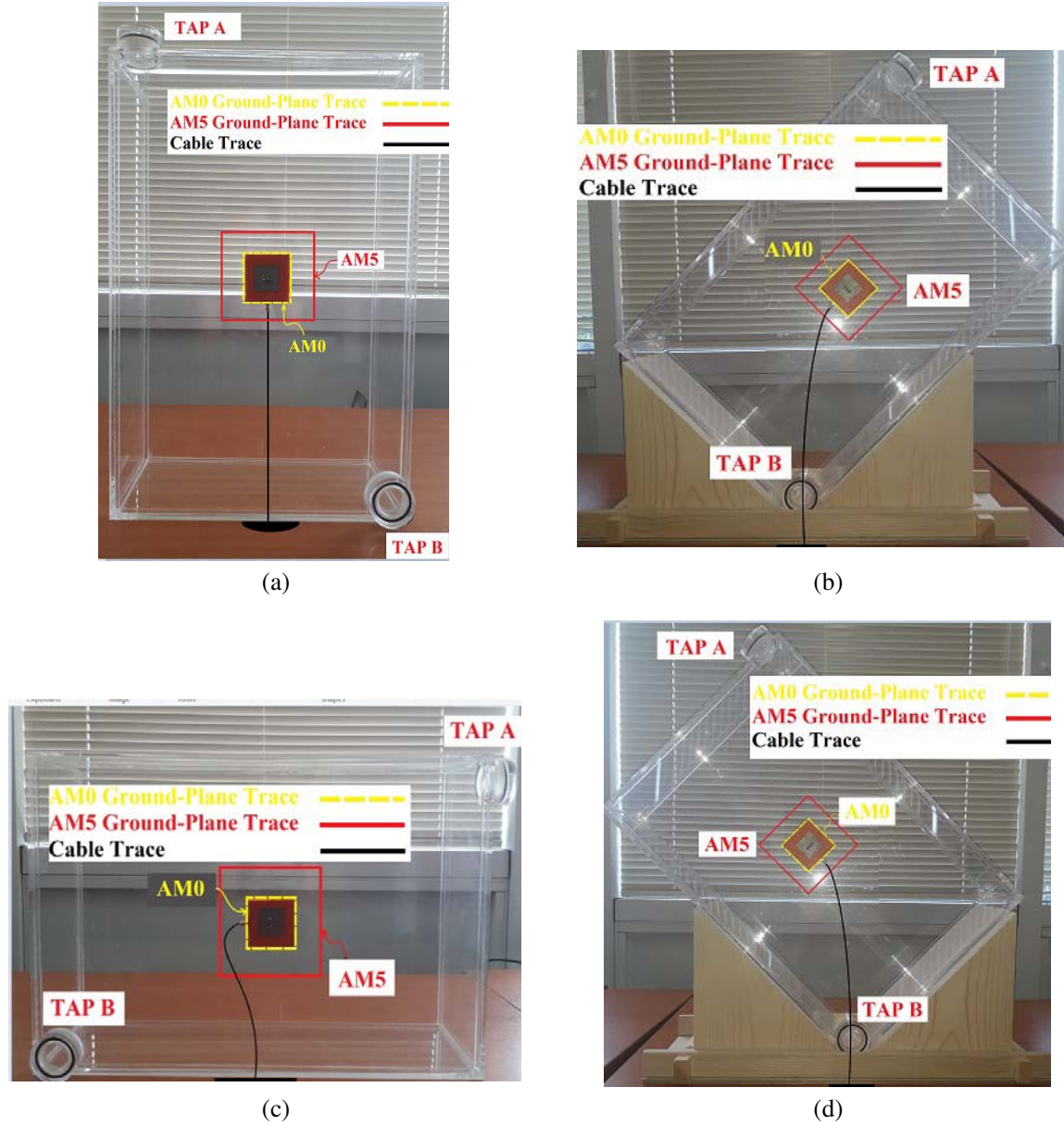
Figure 6. Torso-Phantom, Support Platform, Cable and Ground-plane traces for: (a) $\varphi = 0°$, (b) $\varphi = 45°$, (c) $\varphi = 90°$, (d) $\varphi = 135°$.

the operational frequency is equal to 2.382 GHz for both models. However, when the antenna models are placed on the phantom, the presence of the lossy material (phantom) led to a minor downshift of their operational frequencies (Fig. 9).

The far-field radiation patterns for AM0 and AM5 for each value of φ and all values of θ are depicted in Figs. 10(a)–10(d) and 11(a)–11(d), respectively. Each diagram is similar to that of a dipole antenna oriented normal to the body. The differences between the radiation patterns with (solid line) and without phantom-free space (dotted line) for each φ-value and each antenna model, as well as the ripples in the antenna back-radiation, imply energy absorption by the fabricated phantom. This antenna energy absorption is basically visualized by the size-reduction of the radiation diagram from dotted (free space) to solid (on phantom) curves. Again said in another way, the on-phantom curves are engulfed by the free space curves.

Comparing the pairs of related on-phantom curves of (Figs. 10(a) and 11(a), Figs. 10(b) and 11(b),
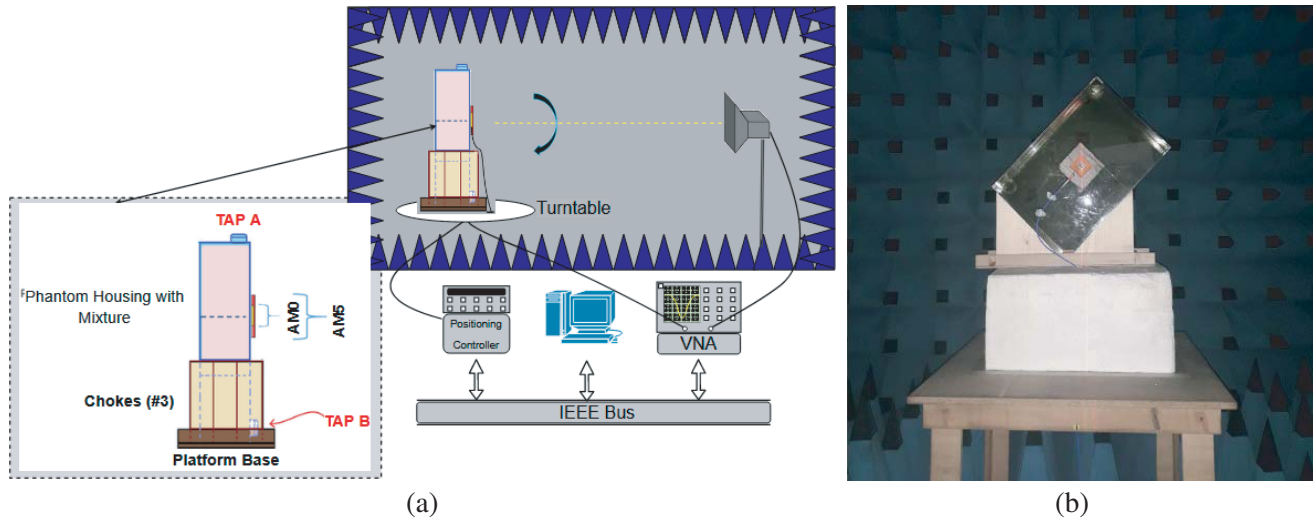
Figure 7. (a) Measurements set-up in the anechoic chamber $\varphi = 45°$. (b) Front view of the phantom with supporting platform onto the turn-table of the anechoic chamber $\varphi = 45°$.

Table 4. Test plan.

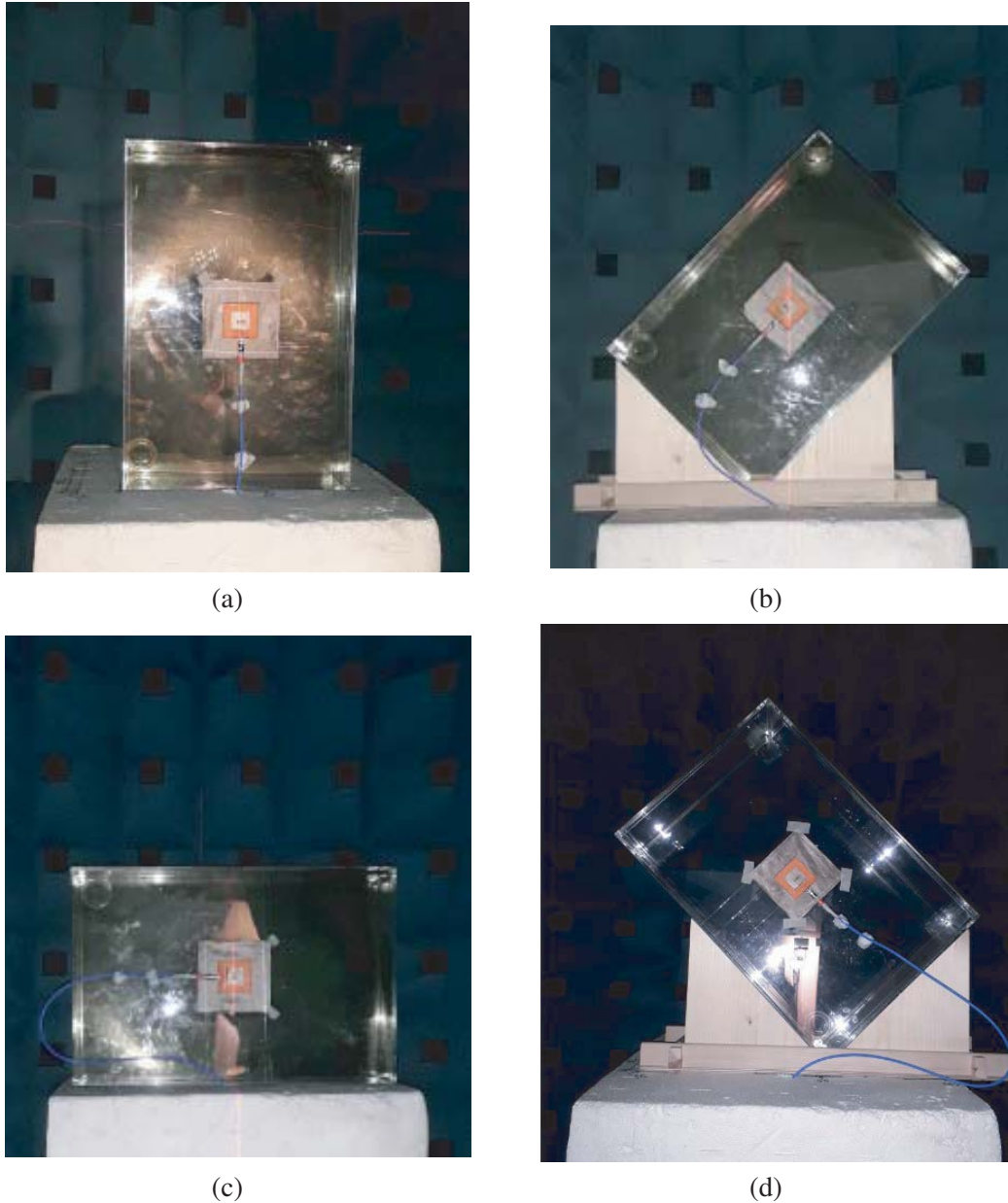| STEPS	Measurements in Free Space (Without Phantom)
1.	**The AUT (AM0, AM5) is aligned at the positioner with the calibrated Horn Antenna by using laser.**
2.	**The Cables of the antennas are calibrated (AM0, EMCO-3115 Horn Antenna) to be removed from final far field measurements.**
3.	$\boldsymbol{\varphi = 0°}$ **and** $\boldsymbol{\theta = 0°, 5°, 15°, 20°, \ldots, 355°}$ **Measurements**
3a.	AM0 → S_{11}, Radiation Diagram for the two components (E_V and E_H components which correspond to the linear Vertical and Horizontal components radiated E-field)
3b.	AM5 → S11, Radiation Diagram for the two components (E_H and E_V components)
4.	$\boldsymbol{\varphi = 90°}$ **and** $\boldsymbol{\theta = 0°, 5°, 15°, 20°, \ldots, 355°}$ **Measurements**
4a.	Repeat Step 3a
4b.	Repeat Step 3b
5.	$\boldsymbol{\varphi = 45°}$ **and** $\boldsymbol{\theta = 0°, 5°, 15°, 20°, \ldots, 355°}$ **Measurements** *(the supportive platform is placed on the turntable and the AUT is re-aligned at the positioner with the calibrated Horn Antenna)*
5a.	Repeat Step 3a
5b.	Repeat Step 3b
6.	$\boldsymbol{\varphi = 135°}$ **and** $\boldsymbol{\theta = 0°, 5°, 15°, 20°, \ldots, 355°}$ **Measurements**
6a.	Repeat Step 3a
6b.	Repeat Step 3b
STEPS	Measurements on Phantom
7.	The phantom liquid is prepared as specified in Section 3.3.
8.	Repeat Steps 3–6

(a)

(b)

(c)

(d)

Figure 8. Measurement procedure: Phantom Position for (a) $\varphi = 0°$, (b) $\varphi = 45°$, (c) $\varphi = 90°$ and (d) $\varphi = 135°$.

Figs. 10(c) and 11(c), Figs. 10(d) and 11(d)), it seems that AM5's performance is less sensitive to the phantom than AM0's because of the larger ground-plane. This confirms simulation findings of our previous work and verifies that a larger ground plane not only can moderate human exposure to EMFs generated by wearable textile patch antennas, but also can maintain acceptable antenna performance. This claim is expected to be confirmed by a decrease in the radiation efficiencies, as well. The two antenna models demonstrate almost equal radiation efficiency in free space scenario: 79.7% for AM0 and 79.8% for AM5 (Table 5). When being located on the phantom, their radiation efficiency drops by 42.4 units (53.2% reduction) for the AM0 and by 29.5 units (36.97% reduction) for the AM5. Consequently, it is concluded that the initial antenna design (AM0) may jointly:

• maintain its performance even with larger ground plane (AM5) in free space scenario, and
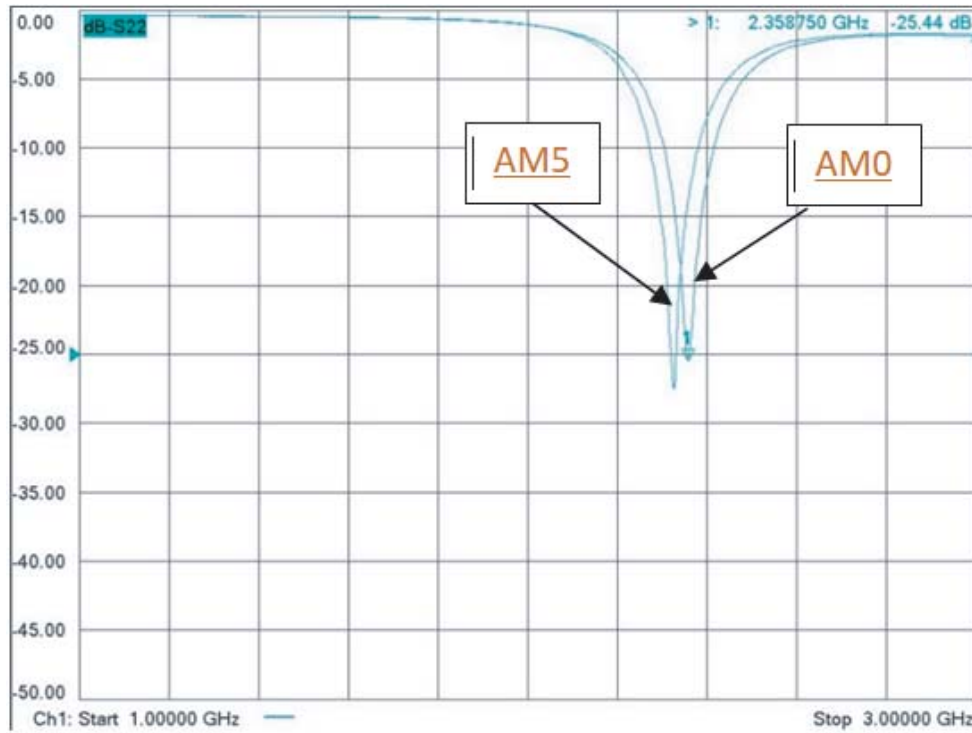• expose the human torso phantom to less EMFs if a larger ground-plane (AM5) is used.

Figure 9. S_{11} on-phantom measurements for AM0 and AM5.

Table 5. Measured radiation efficiencies.

	Free Space	On Phantom
AM0	79.7%	37.3%
AM5	79.8%	50.3%

6. DISCUSSION ON MEASUREMENTS AND PROPOSED METHODOLOGY

EM exposure measurements are usually executed through dedicated special equipment [6]. This solution is fast and more accurate, but it requires expensive dedicate equipment. To maintain the costs low and experiments accurate without loss of generality, we choose to propose a measurements procedure for the estimation of the reduction of the human exposure to wearable EMF sources. The proposed methodology however is based on the estimation of the power absorbed by the torso-equivalent phantom (phantom losses).

Once S_{11} is obtained by the full 2-port S-parameters measurements in the anechoic chamber, the accepted power can be calculated by the following equation for both antenna models:

$$P_{acc} = \left(1 - |S_{11}|^2\right) P_{stim} \tag{7}$$

where P_{stim} is the stimulated power.

The radiation efficiency e_{rad} is basically obtained by the following equation:

$$e_{rad} = \frac{P_{rad}}{P_{acc}} \tag{8}$$

By using this equation P_{stim} and P_{rad} need to be measured accurately which requires extra measurement setups. However, without using any further measurement setup, the radiation efficiency can be also
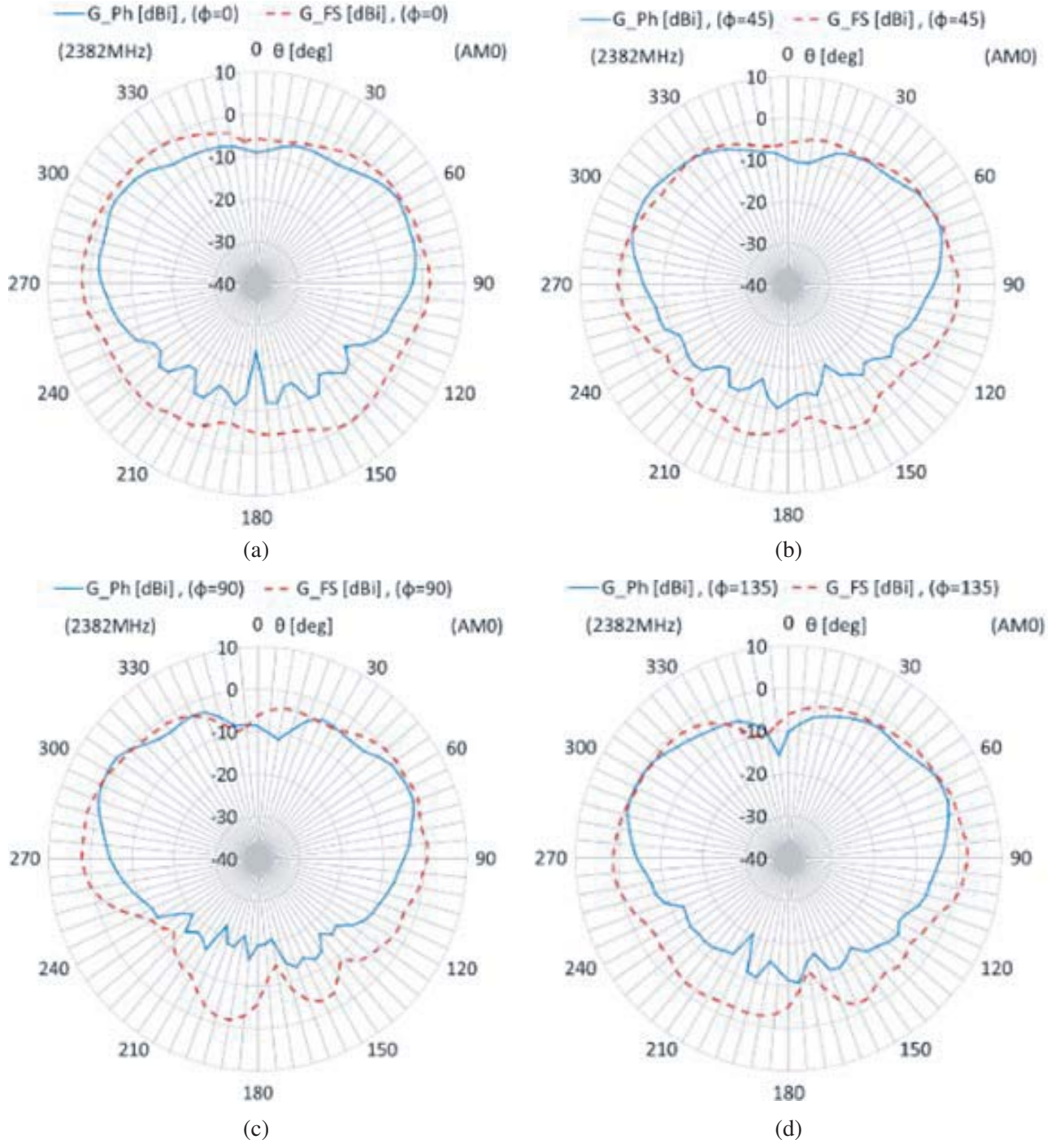
Figure 10. AM0 Radiation Patterns in Free Space (dotted) and on Phantom (solid) for $\theta = 0°, 5°, \ldots, 355°$ and: (a) $\varphi = 0°$, (b) $\varphi = 45°$, (c) $\varphi = 90°$ and (d) $\varphi = 135°$.

obtained by Eq. (9) exploiting the 288 gain — samples (G_i, $i = 1$ to 288 — gain is calculated from S-parameters measurements using a standard Gain Horn) that are obtained through the far field measurements to shape the radiation patterns:

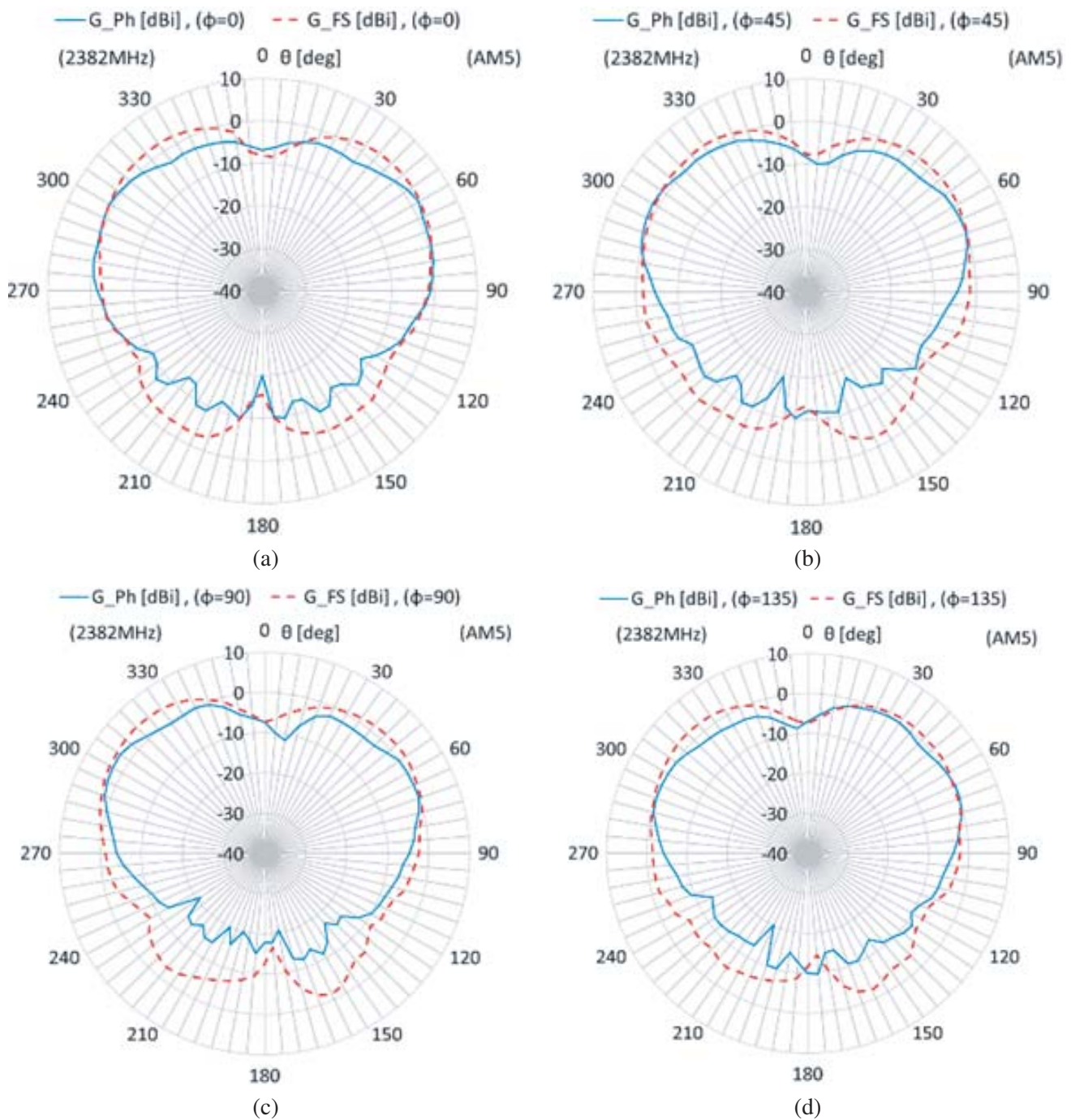$$e_{rad} \approx \frac{1}{4\pi} \sum_\iota G_i \Delta\theta \Delta\varphi \sin\theta_i \tag{9}$$

Figure 11. AM5 Radiation Patterns in Free Space (dotted) and on Phantom (solid) for $\theta = 0°, 5°, \ldots, 355°$ and: (a) $\varphi = 0°$, (b) $\varphi = 45°$, (c) $\varphi = 90°$ and (d) $\varphi = 135°$.

where $\Delta\theta$ (5°) is the step for θ in rad; $\Delta\varphi$ (45°) is the step for φ in rad; G_i is the power gain of the AUT antenna.

The antenna radiation efficiency, as stated above, equals 79.7% for AM0 and 79.8% for AM5 in free space scenario. When the radiation patterns are obtained at the presence of the human phantom ("on-phantom" scenario), the radiation efficiency is 37.3% for AM0 and 50.3% for AM5.

According to the authors in [37], the total absorption coefficient α (Table 6), expressing the

Table 6. Measured total absorption coefficient.

	Free Space (a$_{fs}$)	**On Phantom (a$_{tot}$)**
AM0	20.3%	62.7%
AM5	20.2%	49.7%

percentage of the accepted power that is absorbed in total, is obtained by the radiation efficiency e_{rad} as:

$$a = \frac{Pabs}{P_{acc}} = \frac{P_{acc} - P_{rad}}{P_{acc}} = 1 - \frac{P_{rad}}{P_{acc}} = 1 - e_{rad} \tag{10}$$

It is observed that the absorption coefficients in free space are (almost) equal for the two antennas. These values actually correspond to the antenna losses or — in other words —- to the total power that is absorbed by the antenna materials. To estimate the losses on phantom (power absorbed by the phantom, Table 7), the following equation is used:

$$\alpha_{ph} = a_{tot} - a_{fs} \tag{11}$$

where a_{tot} is the total absorption coefficient when the antenna performance is obtained at the presence of the phantom, while a_{fs} is the total absorption coefficient when the antenna performance is obtained in free space.

Table 7. Measured absorbed power by the phantom.

	α_{ph}
AM0	42.4%
AM5	29.5%
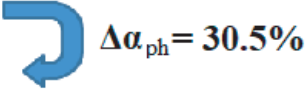
$\Delta\alpha_{ph} = 30.5\%$

As stated above, the latter is practically the absorption coefficient of the antenna. The power absorbed by the phantom is lower when the AM5 is used with regard to the power absorbed by the phantom when the AM0 is used. Thus, it has been proven through the proposed measurement procedure that as the ground-plane increased (e.g., by $\lambda/2$), the absorption of the antenna EM power on the phantom can be reduced (for the specific case, by 30.5%).

In an effort to relate EMF exposure levels as calculated through simulations with our measurements findings, we provide in Table 8 the measured and simulated radiation efficiencies at the presence of the phantom. The small difference between the measured and simulated values for each antenna model could lead to the following assumption: if we were able to measure SAR values, we would see that these values approximate the simulated ones [28].

Table 8. Measured simulated radiation efficiency at the presence of the phantom.

	Simulated	**Measured**
AM0	40.79%	37.3%
AM5	56.96%	50.3%

Overall, it is found that a larger ground-plane indeed leads to a significant reduction of the phantom absorption coefficient. Finally, simulations and measurements were found in good and acceptable agreement (approximately 3%–6% difference); hence the proposed experimental evaluation of the impact of the ground-plane size on the reduction of the power absorbed by the human phantom can be considered as a reliable, simple, and cost-effective method.

7. CONCLUSIONS

Two antenna models with different sizes of ground-plane were fabricated in order to experimentally evaluate the effect of the ground-plane size primarily on the human exposure to their EMFs radiations and — second on their radiation performance. First, a human torso-equivalent phantom was fabricated. The phantom is easy to design and reproduce, and its mechanical and EM properties demonstrate adequate stability. It is made of simple and easily accessible ingredients and materials. Then, we adopted a simple method that is based on common far-field antenna measurements; hence specialized and expensive equipment is not involved. The costs are maintained low, and typical measurements setups are required. More specifically, this method exploits the obtained values of the antennas' radiation efficiency and calculates the total absorption coefficient both in free space and on-phantom. The difference between the coefficients in free space and on phantom provides an estimation of the phantom losses for each antenna. The comparison of the results leads to the conclusion that the larger ground-plane causes a significant 30.5% reduction to the absorbed power by the phantom, while maintaining antenna performance. In addition, the proposed method is easy to reproduce owning to the features and properties of the involved equipment. Finally, our method can be considered as reliable because measurements are in good agreement with simulations.

ACKNOWLEDGMENT

REFERENCES

1. Hombach, V., K. Meier, M. Burkhardt, E. Kuhn, and N. Kuster, "The dependence of EM energy absorption upon human head modeling at 900 MHz," *IEEE Trans. Microwave Theory Tech.*, Vol. 44, 1865–1873, Oct. 1996.

2. Meier, K., V. Hombach, R. Kastle, R. Y.-S. Tay, and N. Kuster, "The dependence of electromagnetic energy absorption upon human head modeling at 1800 MHz," *IEEE Trans. Microwave Theory Tech.*, Vol. 45, 2058–2062, Nov. 1997.

3. Balzano, Q., O. Garay, and T. Manning, "Electromagnetic energy exposure of simulated users of portable cellular telephones," *IEEE Trans. Veh. Technol.*, Vol. 44, 390–403, Aug. 1995.

4. Kobayashi, T., T. Nojima, K. Yamada, and S. Uebayashi, "Dry phantom composed of ceramics and its application to SAR estimation," *IEEE Trans. Microwave Theory Tech.*, Vol. 41, 136–140, Jan. 1993.

5. URL: https://indexsar.com/.

6. URL: https://www.speag.com/products/isar2/isar2-systems/.

7. Sager, M., M. Forcucci, T. Kristensen, "A novel technique to increase the realized efficiency of a mobile phone antenna placed beside a head-phantom," *IEEE Antennas and Propagation Society International Symposium*, Vol. 2, 1013–1016, Columbus, Ohio, USA, Jun. 2003.

8. Holopainen, J., J. Ilvonen, O. Kivekas, R. Valkonen, C. Icheln, and P. Vainikainen, "Near field control of handset antennas based on inverted top wavetraps: Focus on hearing-aid compatibility," *Antennas and Wireless Propagation Letters (AWPL)*, Vol. 8, 592–595, 2009.

9. Picher, C., J. Anguera, A. Andújar, et al., "Analysis of the human head interaction in handset antennas with slotted ground planes," *IEEE Antennas Propag. Mag.*, Vol. 54, No. 2, 36–56, 2012.

10. Andujar, A., J. Anguera, C. Picher, and C. Puente, "Ground plane booster antenna technology. Human head interaction: Functional and biological analysis," *European Conference on Antennas and Propagation, EuCAP 2012*, Prague, Czech Republic, 2012.

11. Nishikido, T., Y. Saito, M. Hasegawa, H. Haruki, Y. Koyanagi, and K. Egawa, "Multi-antenna system for a handy phone to reduce influence by user's hand," *6th International Symposium on Antennas, Propagation and EM Theory, 2003, Proceedings*, 348–351, Beijing, China, 2003.

12. Hirata, A., T. Adachi, and T. Shiozawa, "Folded-loop antenna with a reflector for mobile handset at 2.0 Hz," *Microwave & Opt. Tech. Lett.*, Vol. 40, No. 4, 272–275, 2004.

13. Islam, M. T., M. R. I. Faruque, and N. Misran, "Design analysis of ferrite sheet attachment for SAR reduction in human head," *Progress In Electromagnetics Research*, Vol. 98, 191–205, 2009.

14. Wang, J., O. Fujiwara, and T. Takagi, "Effects of ferrite sheet attachment to portable telephone in reducing electromagnetic absorption in human head," *1999 IEEE International Symposium on Electromagnetic Compatability*, Vol. 2, 822–825, Symposium Record (Cat. No.99CH36261), Seattle, WA, 1999.

15. Hanafi, N. H. M., M. T. Islam, N. Misran, and M. R. I. Faruque, "Numerical analysis of aluminium sheet for SAR reduction," *Proceeding of the 2011 IEEE International Conference on Space Science and Communication (IconSpace)*, 281–285, Penang, 2011.

16. Kwak, S. I., D. U. Sim, J. H. Kwon, and H. D. Choi, "Comparison of the SAR in the human head using the EBG structures applied to a mobile handset," *2007 European Microwave Conference*, 937–940, Munich, 2007.

17. Hwang, J. N. and F. C. Chen, "Reduction of the peak SAR in the human head with metamaterials," *IEEE Transactions on Antennas and Propagation*, Vol. 54, No. 12, 3763–3770, Dec. 2006.

18. Rani, R., P. Kaur, and N. Verna, "Metamaterials and their applications in patch antenna: A review," *International Journal of Hybrid Information Technology*, Vol. 8, No. 11, 199–212, 2015.

19. Yimdjo Poffelie, L. A., P. J. Soh, S. Yan, and G. Vandenbosch, "A high-fidelity all-textile UWB antenna with low back radiation for off-body WBAN applications," *IEEE Transactions on Antennas and Propagation*, Vol. 64, No. 2, 757–760, 2016.

20. Aun, N. F. M., P. J. Soh, A. A. Al-Hadi, M. F. Jamlos, G. A. E. Vandenbosch, and D. Schreurs, "Revolutionizing wearables for 5G: 5G technologies: Recent developments and future perspectives for wearable devices and antennas," *IEEE Microwave Magazine*, Vol. 18, No. 3, 108–124, May 2017.

21. Gil, I. and R. Fernández-García, "SAR impact evaluation on jeans wearable antennas," *2017 11th European Conference on Antennas and Propagation (EUCAP)*, 2187–2190, Paris, 2017.

22. Bhattacharjee, S., M. Mitra, and S. R. Bhadra Chaudhuri, "An effective SAR reduction technique of a compact meander line antenna for wearable applications," *Progress In Electromagnetics Research M*, Vol. 55, 143–152, 2017.

23. Zhong, J., A. Kiourti, T. Sebastian, Y. Bayram and J. L. Volakis, "Conformal load-bearing spiral antenna on conductive textile threads," *IEEE Antennas and Wireless Propagation Letters*, Vol. 16, 230–233, 2017.

24. Wang, K. and J. Li, "Jeans textile antenna for smart wearable antenna," *2018 12th International Symposium on Antennas, Propagation and EM Theory (ISAPE)*, 1–3, Hangzhou, China, 2018.

25. Wang, M., et al., "Investigation of SAR reduction using flexible antenna with metamaterial structure in wireless body area network," *IEEE Transactions on Antennas and Propagation*, Vol. 66, No. 6, 3076–3086, Jun. 2018

26. Pei, R., M. Leach, E. G. Lim, Z. Wang, J. Wang, and Y. Huang, "A belt antenna design with textile aritficial magnetic conductor reflector," *2019 IEEE MTT-S International Wireless Symposium (IWS)*, 1–3, Guangzhou, China, 2019.

27. Seimeni, M. A., A. Tsolis, A. A. Alexandridis, and St. Pantelopoulos, "Mitigation of end-user's exposure to EMF of wearable antennas," *Proceedings of the 14th Conference on Antennas & Propagation (LAPC2018)*, 5 pages, Loughborough, UK, Nov. 12–13, 2018.

28. Seimeni, M. A., A. Tsolis, A. A. Alexandridis, and S. A. Pantelopoulos, "The effects of ground-plane of a textile higher mode microstrip patch antenna on SAR," *2020 International Workshop on Antenna Technology (iWAT)*, 1–4, Bucharest, Romania, 2020.

29. CST Studio Suite, URL: https://www.3ds.com/products-services/simulia/products/cst-studio-suite/solvers/.

30. Gabriel, C., "Compilation of the dielectric properties of body tissues at RF and microwave frequencies," *Brooks Air-Force Base*, report No. AL/OE-TR-1996-0037.

31. URL: http://niremf.ifac.cnr.it/tissprop/htmlclie/htmlclie.php#inizio, accessed May 21st, 2020.

32. Yilmaz, T., R. Foster, and Y. Hao, "Broadband tissue mimicking phantoms and a patch resonator for evaluating noninvasive monitoring of blood glucose levels," *IEEE Transactions on Antennas and Propagation*, Vol. 62, No. 6, 3064–3075, Jun. 2014.

33. Castelló-Palacios, S., A. Vallés-Lluch, C. Garcia-Pardo, A. Fornes-Leal, and N. Cardona, "Formulas for easy-to-prepare tailored phantoms at 2.4 GHz ISM band," *2017 11th International Symposium on Medical Information and Communication Technology (ISMICT)*, 27–31, Lisbon, 2017.

34. Groumpas, E., M. Koutsoupidou, I. S. Karanasiou, C. Papageorgiou, and N. Uzunoglu, "Real-time passive brain monitoring system using near-field microwave radiometry," *IEEE Trans. Biomed. Eng.*, Vol. 67, No. 1, 158–165, 2020.

35. Mobashsher, A. T. and A. M. Abbosh, "Artificial human phantoms: Human proxy in testing microwave apparatuses that have electromagnetic interaction with the human body," *IEEE Microwave Magazine*, Vol. 16, No. 6, 42–62, Jul. 2015.

36. Tsolis, A., A. Paraskevopoulos, A. A. Alexandridis, W. G. Whittow, A. Chauraya, and J. C. Vardaxoglou, "Design, realisation and evaluation of a liquid hollow torso phantom appropriate for wearable antenna assessment," *IET Microwaves, Antennas & Propagation*, Vol. 11, No. 9, 1308–1316, 2017.

37. Zervos, T., A. A. Alexandridis, V. V. Petrovic, et al., "Mobile phone antenna performance and power absorption in terms of handset size and distance from user's head," *Wireless Pers. Commun.*, Vol. 33, 109–120, 2005.